Thermodynamics and Melting of a Quantum Quasicrystal

Ethan C. McGarrigle,[1] Thomas G. Kiely,[2] Leon Balents,[2,3] and Glenn H. Fredrickson[1,4,5,*]
[1]*Department of Chemical Engineering, University of California, Santa Barbara, California 93106, USA*
[2]*Kavli Institute for Theoretical Physics, University of California, Santa Barbara, California 93106, USA*
[3]*Canadian Institute for Advanced Research, Toronto, Ontario M5G 1M1, Canada*
[4]*Materials Research Laboratory, University of California, Santa Barbara, California 93106, USA*
[5]*Materials Department, University of California, Santa Barbara, California 93106, USA*

(Received 23 January 2026; revised 22 May 2026; accepted 1 July 2026; published 3 August 2026)

A quantum quasicrystal was proposed to exist by mean-field, variational arguments in two-dimensional Rashba spin-orbit coupled BECs with dipolar interactions. Despite this remarkable prediction, there is little known about the superfluid character or stability of this quasicrystalline state against thermal and quantum fluctuations, whose importance is implied by the massive single-particle degeneracy of the Rashba Hamiltonian. Here, we apply field-theoretic numerical simulations based on a boson coherent state path integral representation to simulate the finite-temperature behavior of a periodic approximant of an octagonal quasicrystal. We find that the quasicrystal state maintains a 50% superfluid fraction down to low temperature, suggesting supersolid character. We compute a phase diagram that depicts a region of thermodynamic stability for the octagonal quasicrystal phase at low temperature. At intermediate temperature, the quasicrystal undergoes a first-order transition into a crystalline BEC with hexagonal symmetry. Our findings support a possible experimental realization of the octagonal quasicrystal in ^{164}Dy quantum gases below a temperature of 75 nK.

DOI: 10.1103/3646-v33q

Introduction—Quasicrystals are ordered systems with long-range orientational correlations, yet they lack the periodic character and discrete translational invariance of genuine crystals [1,2]. The existence of quasicrystals was controversial until their discovery was confirmed by the simultaneous observation of Bragg peaks as well as rotational symmetries that forbid periodic order (e.g., fivefold, eightfold, tenfold). Since the first discovery of an icosahedral quasicrystal in AlMn alloys [3], quasicrystals have been observed in many classical systems via self-assembly or external driving mechanisms. In soft matter, there are numerous examples in block polymers [4–7] as well as dendrimer micelles [8] and colloids [9]. Quasicrystals have garnered significant attention due their unconventional properties such as low friction and poor conductivity [10], as well as their rich physics, which includes phason excitations and the possibility of topologically distinct variants [11,12].

Quantum quasicrystals are many-body quantum states that display quasicrystalline order. They have been argued to have richer properties, such as additional phason excitations, than their classical counterparts. In bosonic matter, superfluidity and long-range coherence are argued to occur simultaneously with quasicrystalline order, constituting a new type of supersolid [13–17]. Furthermore, recent ultracold quantum gas experiments have used quasicrystalline optical lattice potentials to study localization and disorder effects [18–20]. Nonetheless, experimental observations of a bulk quantum quasicrystal are lacking.

From a theoretical perspective, the understanding of quantum quasicrystals is limited to information gleaned from phenomenological treatments [14,16] or mean-field analyses [13,15]. Here, we investigate a scenario where a quasicrystalline phase emerges naturally in the bulk of a quantum gas system with a realistic dipolar pair potential. Quantum gas experiments provide avenues for realizing physics that elude condensed matter systems, such as pseudospin-$1/2$ bosons with spin-orbit coupling [21,22]. For particles imbued with a two-dimensional isotropic "Rashba" spin-orbit coupling (SOC) with wave vector κ, the single-particle energy $E(\mathbf{k})$ is minimized on a continuous circle of plane-wave states at wave vectors $|\mathbf{k}| = \kappa$ [23–27]. In the case of Bose-Einstein particle statistics, this massive single-particle degeneracy of the Rashba Hamiltonian facilitates Bose-Einstein condensation at multiple wave vectors on the circle, leading to states with broken translation invariance such as stripe phases [23,28,29]. Furthermore, the two-dimensional dipolar interaction is attractive for high-momentum states and thus further promotes condensation into several distinct wave vector states. As a result, a BEC with quasicrystalline order could emerge for strong Rashba SOC with significant dipolar interactions [13].

*Contact author: ghf@ucsb.edu

In this Letter, we investigate an octagonal quantum quasicrystal phase at finite temperature in Rashba spin-orbit coupled, dipolar BECs. Using complex Langevin sampling of the corresponding coherent state field theory, our simulations provide unbiased thermodynamics and include the full spectrum of quantum and thermal fluctuations despite the presence of a sign problem in the Rashba Hamiltonian. Simulated structure factors of the model at low temperature confirm the quasicrystalline nature of the octagonal phase and reveal additional ringlike density correlations via collective excitations. Because of their broken translational symmetry, we observe a significant reduction in superfluidity at low temperature in both the crystalline and quasicrystalline phases, with an overall superfluid fraction of ~50%. As such, our results suggest that the octagonal quasicrystal BEC constitutes a type of supersolid. Lastly, we study the melting behavior of the quasicrystal and other crystalline BEC states, finding a first-order transition from octagonal quasicrystal (QC) to hexagonal BEC. At a higher critical temperature, our simulations reveal the simultaneous loss of superfluid order, Bose-Einstein (quasi)condensation, and quasi-long-range orientational order.

Methods—Our statistical mechanical treatment begins with a second-quantized Hamiltonian $\hat{H} = \hat{H}_{\mathrm{SOC}} + \hat{H}_{\mathrm{int}}$ describing bosons with SOC as well as short-ranged contact and long-ranged dipolar interactions in two dimensions,

$$\hat{H}_{\mathrm{SOC}} = \int d^2r \hat{\Psi}^{\dagger}\left[\frac{1}{2m}(\hat{\boldsymbol{p}}\,\underline{\underline{I}} - \boldsymbol{\mathcal{A}})^2\right]\hat{\Psi}, \tag{1}$$

$$\hat{H}_{\mathrm{int}} = \frac{A^2}{2}\sum_{\alpha\gamma}\sum_{\mathbf{k}}\hat{\rho}_{\alpha,\mathbf{k}},\eta_{\alpha\gamma}u(\mathbf{k})\hat{\rho}_{\gamma,-\mathbf{k}}, \tag{2}$$

where $\hat{\Psi} = [\hat{\psi}_{\uparrow}(\mathbf{r}), \hat{\psi}_{\downarrow}(\mathbf{r})]^T$ is a two-component vector of second-quantized Bose field operators in the pseudospin-1/2 basis [30], $A = L_x L_y$ is the area of the bulk gas in a cell with dimensionality $L_x \times L_y$, and $\hat{\rho}_{\alpha,\mathbf{k}} = \hat{\psi}^{\dagger}_{\alpha,\mathbf{k}}\hat{\psi}_{\alpha,\mathbf{k}}$ is a microscopic density operator for pseudospin α with Fourier component labeled by wave vector $\mathbf{k}$, where $k_\nu = 2\pi m_\nu/L_\nu$ is the ν th component and $m_\nu \in \mathbb{Z}$. The vector potential $\boldsymbol{\mathcal{A}} = \hbar\kappa(\underline{\underline{\sigma}}^x, \underline{\underline{\sigma}}^y)$ prescribes Rashba SOC with strength κ and admits a circle of single-particle energy minima at $|\mathbf{k}| = \kappa$. $\eta_{\alpha\gamma}$ parametrizes the miscibility of pseudospins; however, we work in the regime of spin-independent interactions $\eta_{\alpha\gamma} = 1$, which may correspond with high-spin states of ^{164}Dy [13], finding that minor variations away from $\eta_{\alpha\gamma} = 1$ do not qualitatively change our results.

Atoms or molecules with permanent dipoles oriented in the axial ($\hat{z}$) direction lead to an effective two-dimensional interaction potential $u(\mathbf{k}) = u_0[1 - R|\mathbf{k}|d_z w(|\mathbf{k}|d_z/\sqrt{2})]$ with $w(x) = \mathrm{erfc}(x)e^{x^2}$ and $d_z = \sqrt{\hbar/m\omega_z}$ the length scale set by strong axial ($\hat{z}$) harmonic confinement [31–33]. The behavior of $u(\mathbf{k})$ is characterized by two parameters: (1) an overall strength $u_0 \equiv g_{3D}(1 + 2\epsilon_{\mathrm{dd}})/(\sqrt{2\pi}d_z)$, where $g_{3D} = 4\pi\hbar^2 a_s/m$ with s-wave scattering length a_s; and (2) a dipolar parameter $R = (3/2)\sqrt{\pi/2}[1 + (2\epsilon_{\mathrm{dd}})^{-1}]^{-1}$ in which $\epsilon_{\mathrm{dd}} \equiv C_d/3g_{3D}$ characterizes the strength of dipolar interactions relative to contact interactions, where $C_d = \mu_D^2\mu_0$ ($C_d = d_e^2/\epsilon_0$) for magnetic (electric) dipoles with moment μ_D (d_e) [32].

The case of $R > \sqrt{\pi/2} \equiv R^*$ corresponds to dominant dipolar interactions where attractive scattering processes become important. To investigate the model's universal behavior, we rescale all wave vectors, spatial coordinates, and fields by the BEC healing length $\ell = (\hbar^2/2m\mu_{\mathrm{eff}})^{1/2}$ [32], which yields a dimensionless Hamiltonian $\hat{\mathcal{H}} = \hat{H}/\mu_{\mathrm{eff}}$ with effective chemical potential $\mu_{\mathrm{eff}} \equiv \mu - \hbar^2\kappa^2/m$. Our scaling choice yields a set of governing dimensionless parameters: $\bar{\kappa} = \kappa\ell$, $\bar{g} = u_0 2m/\hbar^2$, $\overline{d_z} = d_z/\ell$.

For thermodynamics at dimensionless temperature $\overline{T} = \bar{\beta}^{-1} \equiv k_B T/\mu_{\mathrm{eff}}$, we build a grand canonical partition function $\mathcal{Z}(\mu, A, T) = \mathrm{Tr}[e^{-\bar{\beta}\hat{\mathcal{H}} + \bar{\beta}\hat{N}}]$, factorizing the exponential into N_τ slices with imaginary time discretization $\Delta_\tau = \bar{\beta}/N_\tau$. As in our previous work [34], we express the partition function as a path integral over imaginary time segments $j = 0, 1, \ldots, N_\tau - 1$ using a basis of dressed coherent states $\tilde{\boldsymbol{\phi}}_{j,\mathbf{k}} \equiv [\tilde{\phi}_+, \tilde{\phi}_-]^T_{j,\mathbf{k}} = U_{\mathbf{k}}\boldsymbol{\phi}_{j,\mathbf{k}}$, $\tilde{\boldsymbol{\phi}}^{\dagger}_{j,\mathbf{k}} \equiv [\tilde{\phi}^*_+, \tilde{\phi}^*_-]_{j,\mathbf{k}} = U^{\dagger}_{\mathbf{k}}\boldsymbol{\phi}^{\dagger}_{j,\mathbf{k}}$. This path integral uses an exact treatment of the SOC kinetic propagator on a dressed coherent state after a unitary transformation $U_{\mathbf{k}}$ from the pseudospin basis. The dressed coherent states obey periodic boundary conditions in imaginary time and correspond to helicity states $|\pm; \mathbf{k}\rangle$ with dispersion $D_{\mathbf{k}}(\pm) = \mathbf{k}^2 \pm 2|\mathbf{k}|\bar{\kappa}$.

An interacting field theory that is first-order accurate in Δ_τ emerges from the path-integral procedure, consisting of functional integrals over dressed coherent state fields $\mathcal{Z} = \int \mathcal{D}(\tilde{\boldsymbol{\phi}}, \tilde{\boldsymbol{\phi}}^{\dagger})e^{-S[\tilde{\boldsymbol{\phi}}, \tilde{\boldsymbol{\phi}}^{\dagger}]}$, weighted by an action functional $S[\tilde{\boldsymbol{\phi}}, \tilde{\boldsymbol{\phi}}^{\dagger}]$,

$$\begin{aligned} S[\tilde{\boldsymbol{\phi}}, \tilde{\boldsymbol{\phi}}^{\dagger}] = &\sum_{\alpha}\sum_{j}\sum_{\mathbf{k}}\tilde{\phi}^*_{\alpha,j,\mathbf{k}}[\tilde{\phi}_{\alpha,j,\mathbf{k}} - e^{-\Delta_\tau D_{\mathbf{k}}(\alpha)}\tilde{\phi}_{\alpha,j-1,\mathbf{k}}] \\ &+ \frac{\bar{\beta}}{2N_\tau}\sum_{\alpha,\gamma}\sum_{j}\int d^2r\int d^2r'\phi^*_{\alpha,j}(\mathbf{r})'\phi^*_{\gamma,j}(\mathbf{r}')' \\ &\times u(|\mathbf{r} - \mathbf{r}'|)\phi'_{\gamma,j-1}(\mathbf{r}')\phi'_{\alpha,j-1}(\mathbf{r}), \end{aligned} \tag{3}$$

where $\boldsymbol{\phi}'_{j,\mathbf{k}} = U^{\dagger}_{\mathbf{k}}e^{-\Delta_\tau D_{\mathbf{k}}}\tilde{\boldsymbol{\phi}}_{j,\mathbf{k}}$ and $(\boldsymbol{\phi}^{\dagger})'_{j,\mathbf{k}} = U_{\mathbf{k}}e^{-\Delta_\tau D_{\mathbf{k}}}\tilde{\boldsymbol{\phi}}^{\dagger}_{j,\mathbf{k}}$ denote coherent state field vectors in the pseudospin basis after forward propagation in imaginary time by the SOC kinetic propagator [34].

To investigate thermodynamic properties and phase behavior of the dipolar, spin-orbit coupled boson ensemble, we employ a field-theoretic simulation technique [35] that

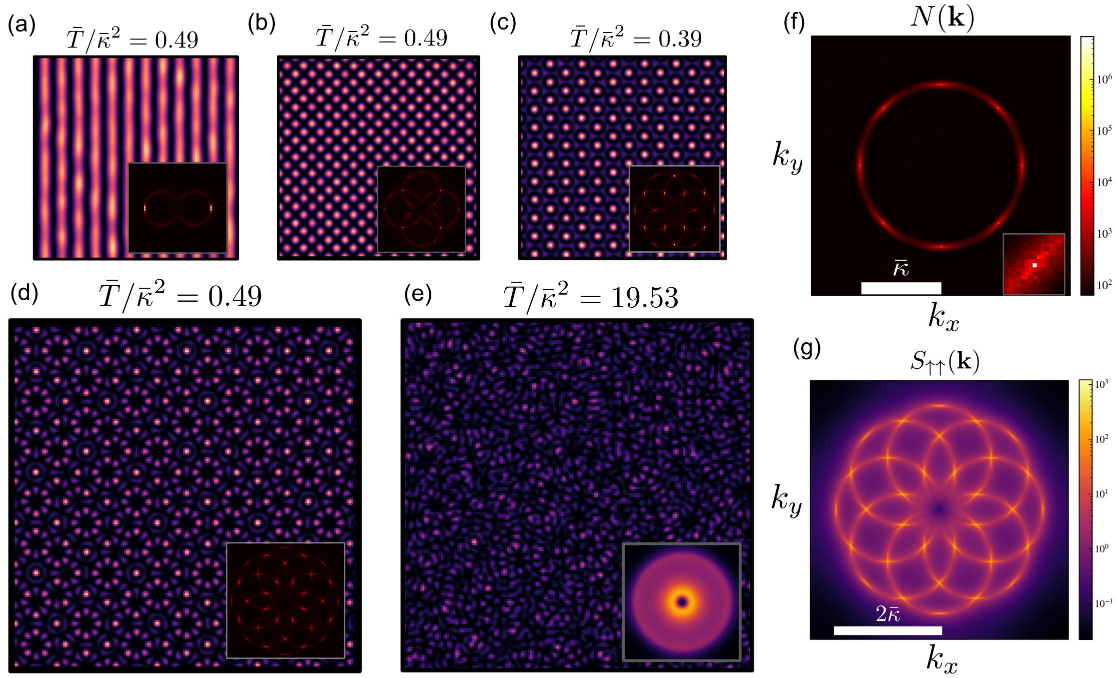

FIG. 1. Equilibrium phases in dipolar BECs with strong Rashba spin-orbit coupling $\bar{\kappa} = 16$ with dominant dipolar interactions $R > \sqrt{\pi/2}$ and with $\bar{g} = 0.01$ and $\bar{d}_z = 1$. Snapshots of the density profile $\rho_{\uparrow}(\mathbf{r})$ for atoms in the $|\uparrow\rangle$ pseudospin state in the low-temperature (a) stripe phase ($R = 1.24$), (b) square crystalline phase ($R = 1.26$), (c) hexagonal phase ($R = 1.267$), (d) octagonal quasicrystal phase ($R = 1.272$), and (e) the high-temperature isotropic fluid phase ($R = 1.272$). For each density pattern, the corresponding static structure factor $S_{\uparrow\uparrow}(\mathbf{k})$ is plotted on a linear intensity scale and shown in the inset, reflecting the rotational symmetry of each structure. (f) Momentum distribution $N(\mathbf{k})$ and (g) diagonal static density structure factor $S_{\uparrow\uparrow}(\mathbf{k})$ of the octagonal quasicrystal at $\bar{T}/\bar{\kappa}^2 = 0.49$ and $R = 1.272$, depicting density correlations for atoms in the $|\uparrow\rangle$ pseudospin state. The inset of (f) shows an example Bose-condensed peak in the white pixel. Intensity is plotted on a logarithmic scale to reveal excitations around the Bose-condensed and Bragg peaks in (f) and (g), respectively.

leverages a fictitious complex Langevin dynamics to sample $\tilde{\boldsymbol{\phi}}$, $\tilde{\boldsymbol{\phi}}^{\dagger}$ configurations according to the non-positive-definite distribution e^{-S}. Details of the Langevin algorithm and field-theoretic simulation convergence parameters are discussed in End Matter. From the simulation dynamics, unbiased thermal expectation values of operators $\langle \hat{O} \rangle$ are recovered by sample-averaging corresponding observable functionals $O[\boldsymbol{\phi}, \boldsymbol{\phi}^{\dagger}]$ with respect to the Langevin process.

Equilibrium phases are identified by examining snapshots of the pseudospin density profiles $\rho_{\alpha}[\phi, \phi^*; \mathbf{r}] = 1/N_{\tau} \sum_{j=0}^{N_{\tau}-1} \phi^*_{\alpha,j}(\mathbf{r})' \phi'_{\alpha,j-1}(\mathbf{r})$ as well as expectation values of the momentum distribution $\tilde{N}[\boldsymbol{\phi}, \boldsymbol{\phi}^{\dagger}; \mathbf{k}] = A/N_{\tau} \sum_{\alpha} \sum_{j=0}^{N_{\tau}-1} (\phi^*_{\alpha,-\mathbf{k}})' \phi'_{\alpha,\mathbf{k}}$. Additionally, the static density structure factor $S_{\alpha\gamma}(\mathbf{k}) = \langle \rho_{\alpha,\mathbf{k}} \rho_{\gamma,-\mathbf{k}} \rangle - \langle \rho_{\alpha,\mathbf{k}} \rangle \langle \rho_{\gamma,-\mathbf{k}} \rangle$ enables investigation of density-density correlations, where $\rho_{\alpha,\mathbf{k}}$ is the spatial Fourier transform of $\rho_{\alpha}(\mathbf{r})$. Both the momentum distribution and structure factor provide a straightforward identification of Bose-condensed states with M-fold rotational symmetry. Additionally, the superfluid stiffness tensor is estimated via a phase twist approach [36,37],

$$\rho_{\mathrm{SF}}^{\mu\nu} = \delta_{\mu\nu} \langle N \rangle / A - (\bar{\beta}/A)[\langle P_{\mu} P_{\nu} \rangle - \langle P_{\mu} \rangle \langle P_{\nu} \rangle], \quad (4)$$

where $\mu, \nu \in \{x, y\}$ and the total particle number $\langle N \rangle$ and physical momentum vector $\langle \mathbf{P} \rangle$ are computed using methods in Ref. [37].

Low-temperature phase behavior—Langevin simulations find that the low-temperature phase behavior of the strongly spin-orbit coupled, dipolar BEC system aligns qualitatively with the mean-field results of Ref. [13]. Above R^*, BEC states with crystalline order appear with lower free energy compared to the superfluid stripe phase. Figure 1 provides density profiles of each phase. With increasing R at fixed temperature, ordered structures with square [Fig. 1(b)], hexagonal symmetry [Fig. 1(c)], and octagonal symmetry [Fig. 1(d)] are depicted, with their corresponding structure factor patterns shown in the insets with a linear scale. The static structure factor inset of Fig. 1(d) supplies a key verification of the quasicrystal state—the simultaneous presence of Bragg peaks as well as an eightfold rotational symmetry that forbids periodic order. Additionally, each momentum distribution consists of M sharply peaked points for the M-fold symmetric state, as shown in Fig. 1(f). These structures thus represent highly fragmented BECs with density modulations that reflect the M-fold rotational symmetry breaking of the ground state.

Langevin simulations reveal the consequential role of fluctuations at low temperature. Figure 1(g) shows a rich fluctuation spectrum in the $|\uparrow\rangle$ diagonal structure factor, with intensity plotted on a logarithmic scale. Overlapping circles of intensity with radius $\bar{\kappa}$ map out the spectrum of low-energy excitations, which inherit the noninteracting Rashba dispersion but are now centered about the condensed momenta $\mathbf{k}_m = \bar{\kappa}(\cos\theta_m, \sin\theta_m)$ for an M-fold symmetric structure, with $\theta_m = 2\pi(m-1)/M$ with $m = 1, 2, \ldots, M$. This displaced ring dispersion is consistent with the excitation spectrum derived from a Bogoliubov expansion [33,38,39]. Ultimately, the density profiles at low temperature are consistent with constructive interference of the BEC wave functions at different momenta, and the density correlations decay for wave vectors $|\mathbf{k}| > 2\bar{\kappa}$. We observe qualitatively the same results when comparing structure factor components $S_{\uparrow\uparrow}(\mathbf{k})$, $S_{\downarrow\downarrow}(\mathbf{k})$, and the total density structure factor $S_{\mathrm{tot}}(\mathbf{k}) = \langle\rho_{\mathbf{k}}\rho_{-\mathbf{k}}\rangle - \langle\rho_{\mathbf{k}}\rangle\langle\rho_{-\mathbf{k}}\rangle$.

In both the periodic and quasiperiodic states, complex Langevin simulations reveal a significant reduction in superfluidity down to low temperature, shown in Fig. 2(b). Although the vertically oriented stripe phase in Fig. 1(a) is highly anisotropic with $\rho_{\mathrm{SF}}^{xx}/\rho \to 1$ and $\rho_{\mathrm{SF}}^{yy}/\rho \ll 1$ at low temperature, the overall superfluid fraction $\rho_{\mathrm{SF}}/\rho = (\rho_{\mathrm{SF}}^{xx} + \rho_{\mathrm{SF}}^{yy})/2\rho$ is consistent at approximately 46% to 50% across all the Bose-condensed, ordered mesophases and shows little R or system size dependence. The significant reduction in superfluidity down to low temperature is consistent with strong fluctuations and the presence of low-energy excitations along surfaces with momenta $|\mathbf{k} - \mathbf{k}_m| = \bar{\kappa}$ about each of the condensed peaks at $\mathbf{k}_m$. Furthermore, the superfluid fraction shows no statistically significant variation among the different mesophases at fixed temperature, suggesting that the phason excitations in the octagonal quasicrystal are coherent and do not disrupt bulk superfluidity.

Thus, our simulations suggest that the phases in Fig. 1 garner supersolid character, defined by simultaneous superfluidity [Fig. 2(b)] and broken translational symmetry (Fig. 1). Although SOC and dipolar interactions can individually bring forth supersolid phases, the Rashba SOC constrains the possible supersolid structures by restricting allowed condensed wave vectors to $|\mathbf{k}| = \bar{\kappa}$. The dipolar interactions then promote structures with further rotational symmetry breaking.

Phase transitions—To identify the globally stable mesophase at finite temperature, the grand free energy $\Omega = \beta^{-1}\ln[\mathcal{Z}]$ is computed directly for each phase of interest via $\Omega = -PA$, with details in [33,40]. Figure 2(a) depicts the grand free energies as a function of the dipolar parameter R at fixed temperature. At low-temperature, mean-field theory predicts phase boundaries between M and $(M+2)$-fold

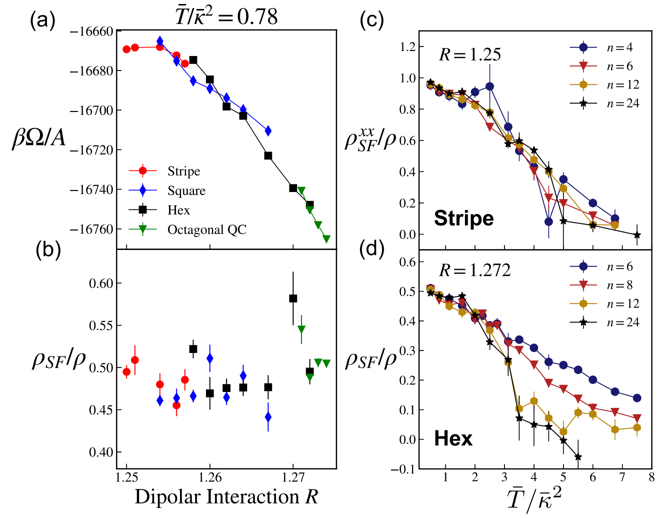

FIG. 2. Phase transitions: First-order phase boundaries are determined by the grand free energy, while thermal phase transitions are marked by the decay of the superfluid density with increasing temperature. (a) Grand free energy of the stripe (red circles), square-packed BEC (blue diamonds), hexagonal-packed BEC (black squares), and octagonal quasicrystal BEC (green triangles) with varying R at fixed temperature. (b) Superfluid fraction for each low-temperature mesophase. (c) $\hat{x}$ component of the superfluid stiffness for the stripe phase at $R = 1.25$, and (d) overall superfluid fraction of the hexagonal phase at $R = 1.272$ for differing system sizes denoted by the number of periods $n = \bar{\kappa}\bar{L}/2\pi$.

symmetric structures when adding two condensed states becomes energetically favorable, which occurs at

$$R_M = \frac{1}{\Delta k_M d_z w(\Delta k_M d_z/\sqrt{2})}, \tag{5}$$

with $\Delta k_M = \kappa\sin(\pi/M)$. For the strong SOC considered ($\bar{\kappa}\bar{d}_z = 16$), the relevant first-order phase transitions occur near $R \sim 1.25$–1.275; we omit the octagonal-dodecagonal QC transition expected to occur at $R \approx 1.285$ in this work but emphasize that Eq. (5) provides a guide to study other QC phases with $M > 8$. ^{164}Dy quantum gases naturally achieve $R > 1.38$ and would exhibit the mesophases depicted in Fig. 1 near $\bar{\kappa}\bar{d}_z \sim 4$. The End Matter provides details of a possible realization of this model in ^{164}Dy with a hex-QC transition temperature near 75 nK.

The value of R where the (grand) free energies intersect determines the phase boundary between two competing phases, depicting a first-order transition with a jump in orientational order. Figure 2(a) provides evidence of the first-order character of these transitions, namely (1) a discontinuous first derivative of the free energy at each phase boundary, and (2) discontinuous orientational order across each phase boundary.

Figure 3 shows a phase diagram in the $\bar{T}$-R plane, characterizing the equilibrium behavior of two-dimensional

BECs with strong Rashba spin-orbit coupling in the dominant dipolar interaction limit $R > R^*$. Notably, the octagonal QC phase is globally stable for a limited range of temperatures until undergoing a first-order transition into the hexagonal BEC, depicted by free energy data in Fig. 2(a). Field-theoretic simulations show no evidence of a second-order, critical transition between the hexagonal and octagonal BECs; the octagonal BEC retains metastability at increasing temperature until undergoing the critical, second-order phase transition into the isotropic at $\bar{T}/\bar{\kappa}^2 \sim 3$. Supplemental Material [33] probes the hexagonal-octagonal phase boundary at low temperature ($\bar{T}/\bar{\kappa}^2 = 0.49$) with two methods: (1) the converged Langevin method ($\Delta_\tau \ll 1$), and (2) the classical field approximation ($N_\tau = 1$, with Langevin noise). The classical field method captures predominantly thermal fluctuations and erroneously predicts global stability for the hexagonal phase at $R \geq 1.27$, supporting the phase diagram's conclusion that thermal fluctuations destabilize the octagonal QC phase relative to the hexagonal phase.

Raising the temperature ultimately induces melting of the superfluid phases at a critical temperature $\bar{T}_c$. This transition into the isotropic state is second-order, characterized by a diverging correlation length as $\bar{T} \to \bar{T}_c$. As such, finite-size analysis of the superfluid fraction in [33] enables estimation of a precise critical temperature, assuming a Kosterlitz-Thouless-like transition with a universal jump relation modified by the strong SOC [41]. Figures 2(c) and 2(d) show superfluid density data for both the stripe and hexagonal phases at various system sizes, denoted with number of periods n. The superfluid fraction experiences a sharper decline with greater finite-size variations in the hexagonal phase compared to the more fluidlike stripe phase. An analysis of the complex interplay of defects in pseudospin, superfluid phase, and density is deferred to future work, along with a search for a possible hexatic intermediate [42] between the hexagonal BEC and the normal fluid isotropic.

Above $\bar{T}_c$ and at $R \gtrapprox R^*$, the isotropic phase resembles an amorphous droplet fluid with short-ranged positional and orientational order. The corresponding density structure factor in the inset of Fig. 1(e) reveals a broad distribution of droplet sizes due to the dipolar interaction and considerable thermal fluctuations. Although not shown in Fig. 3, the amorphous fluid would eventually cross over into a homogeneous, classical gas at large $\bar{T} \gg \bar{T}_c$, similar to previous studies on Rashba spin-orbit coupled bosons with short-ranged interactions [36,37]. In the short-ranged interaction regime $R \ll R^*$, a pseudospin microemulsion depicted in [36] appears, resembling bicontinuous microemulsions found in classical soft matter systems [43].

Conclusion—We have unveiled the fate of a quantum quasicrystal phase with supersolid character found in dipolar Bose gases with strong Rashba SOC. Although the QC phase is globally stable at the lowest temperatures,

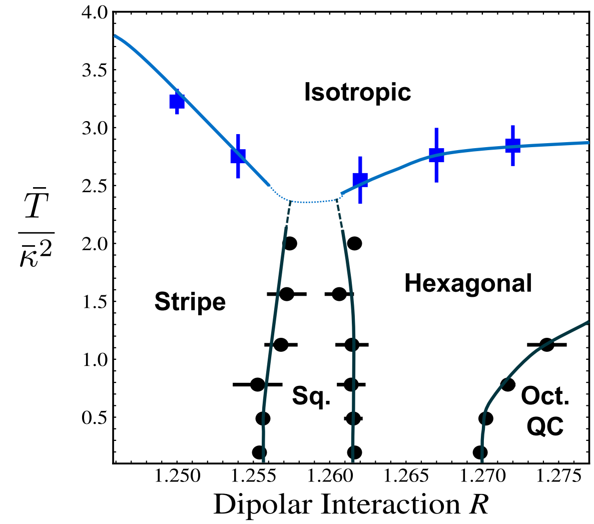

FIG. 3. Finite-temperature phase diagram in the $\bar{T}$-R plane for strongly spin-orbit coupled ($\bar{\kappa}\bar{d}_z = 16$) dipolar bosons in two dimensions, with bare interaction strength $\bar{g} = 0.01$. "SQ" denotes the square-packed crystalline phase with fourfold symmetry, while "Oct. QC" denotes an octagonal quantum quasicrystal phase. Phase boundaries are determined using the free energy and superfluid fraction, with finite-size analysis and discussion of error bars detailed in Supplemental Material [33]. Dashed lines denote an anticipated phase boundary where better statistics are required for accurate determination.

thermal fluctuations produce a first-order transition into the hexagonal BEC state at a temperature lower than the superfluid-normal fluid transition. Furthermore, our simulations reveal a suppression in the superfluid fraction for all crystalline and quasicrystalline BEC states as well as robust low-energy excitations in the static structure factor. These observations highlight the prominent role of fluctuations characteristic of the Rashba Hamiltonian combined with dipolar interactions, which yield a rich spectrum of collective modes that inherit the Rashba dispersion. Above the superfluid transition temperature, an isotropic microemulsion analog appears with normal fluid droplets of distinct pseudospin.

Complementing the analysis in [13], our phase diagram suggests that an experimental realization of the self-assembled quasicrystal phase could be achievable in dysprosium BECs. Moreover, it may be possible to realize a quantum quasicrystal by an inherently nonequilibrium route, such as a rapid temperature quench. For instance, a stochastic Gross Pitaevski simulation report on spin-orbit coupled $S = 1$ BECs suggests that square-packed skyrmion states are achievable via a rapid temperature quench [44]. A similar approach was employed in classical block copolymer experiments, which observed quasicrystalline phases confirmed in x-ray scattering characterization experiments [6,45]. Lastly, a characterization of the phason excitations in the QC phase found in Rashba spin-orbit coupled, dipolar BECs is still needed. Such a comparison may involve comparing the real-time Green's function or dynamical structure factor of each low-temperature crystalline phase, requiring a nonequilibrium formalism.

Acknowledgments—This work was enabled by field-theoretic simulation tools developed under support of G. H. F. from the National Science Foundation (CMMT Program, No. DMR-2104255). Use was made of computational facilities purchased with funds from the NSF (No. CNS-1725797) and administered by the Center for Scientific Computing (CSC). The CSC is supported by the California NanoSystems Institute and the Materials Research Science and Engineering Center (MRSEC; NSF No. DMR 2308708) at UC Santa Barbara. This work made use of the BioPACIFIC Materials Innovation Platform computing resources of the National Science Foundation Award No. DMR-2445868. E. C. M is supported by a Mitsubishi Chemical Fellowship, and L. B. is supported by the NSF CMMT program under Grant No. DMR-2419871. T. G. K. acknowledges support from the Gordon and Betty Moore Foundation under No. GBMF7392 and from the National Science Foundation under Grant No. PHY-2309135 to the Kavli Institute for Theoretical Physics.

Data availability—The data that support the findings of this article are openly available [46].

[1] D. Levine and P. J. Steinhardt, Phys. Rev. Lett. **53**, 2477 (1984).
[2] C. Janot and C. Janot, *Quasicrystals: A Primer*, Monographs on the Physics and Chemistry of Materials (Oxford University Press, Oxford, New York, 1992).
[3] D. Shechtman, I. Blech, D. Gratias, and J. W. Cahn, Phys. Rev. Lett. **53**, 1951 (1984).
[4] T. M. Gillard, S. Lee, and F. S. Bates, Proc. Natl. Acad. Sci. U.S.A. **113**, 5167 (2016).
[5] C. R. Iacovella, A. S. Keys, and S. C. Glotzer, Proc. Natl. Acad. Sci. U.S.A. **108**, 20935 (2011).
[6] M. W. Schulze, R. M. Lewis, J. H. Lettow, R. J. Hickey, T. M. Gillard, M. A. Hillmyer, and F. S. Bates, Phys. Rev. Lett. **118**, 207801 (2017).
[7] K. Hayashida, T. Dotera, A. Takano, and Y. Matsushita, Phys. Rev. Lett. **98**, 195502 (2007).
[8] X. Zeng, G. Ungar, Y. Liu, V. Percec, A. E. Dulcey, and J. K. Hobbs, Nature (London) **428**, 157 (2004).
[9] Y. Gao, B. Sprinkle, D. W. M. Marr, and N. Wu, Nat. Phys. **21**, 966 (2025).
[10] C. Zhou, F. Cai, H. Xu, and S. Gong, Mater. Sci. Eng. **386**, 362 (2004).
[11] D. V. Else, S.-J. Huang, A. Prem, and A. Gromov, Phys. Rev. X **11**, 041051 (2021).
[12] Y. E. Kraus, Y. Lahini, Z. Ringel, M. Verbin, and O. Zilberberg, Phys. Rev. Lett. **109**, 106402 (2012).
[13] S. Gopalakrishnan, I. Martin, and E. A. Demler, Phys. Rev. Lett. **111**, 185304 (2013).
[14] A. Mendoza-Coto, M. Bonifacio, and F. Piazza, Phys. Rev. Lett. **134**, 136003 (2025).
[15] J. Hou, H. Hu, K. Sun, and C. Zhang, Phys. Rev. Lett. **120**, 060407 (2018).
[16] G. Pupillo, P. Ziherl, and F. Cinti, Phys. Rev. B **101**, 134522 (2020).
[17] Z. Zhu, H. Yao, and L. Sanchez-Palencia, Phys. Rev. Lett. **130**, 220402 (2023).
[18] J.-C. Yu, S. Bhave, L. Reeve, B. Song, and U. Schneider, Nature (London) **633**, 338 (2024).
[19] K. Viebahn, M. Sbroscia, E. Carter, J.-C. Yu, and U. Schneider, Phys. Rev. Lett. **122**, 110404 (2019).
[20] T. Shimasaki, M. Prichard, H. E. Kondakci, J. E. Pagett, Y. Bai, P. Dotti, A. Cao, A. R. Dardia, T.-C. Lu, T. Grover, and D. M. Weld, Nat. Phys. **20**, 409 (2024).
[21] Y.-J. Lin, K. Jiménez-García, and I. B. Spielman, Nature (London) **471**, 83 (2011).
[22] J.-R. Li, J. Lee, W. Huang, S. Burchesky, B. Shteynas, F. Ç. Top, A. O. Jamison, and W. Ketterle, Nature (London) **543**, 91 (2017).
[23] N. Goldman, G. Juzeliūnas, P. Öhberg, and I. B. Spielman, Rep. Prog. Phys. **77**, 126401 (2014).
[24] A. Manchon, H. C. Koo, J. Nitta, S. M. Frolov, and R. A. Duine, Nat. Mater. **14**, 871 (2015).
[25] K. Wu, J. Chen, H. Ma, L. Wan, W. Hu, and J. Yang, Nano Lett. **21**, 740 (2021).
[26] Y. A. Bychkov and E. I. Rashba, J. Phys. C **17**, 6039 (1984).
[27] T. A. Sedrakyan, A. Kamenev, and L. I. Glazman, Phys. Rev. A **86**, 063639 (2012).
[28] S. Sinha, R. Nath, and L. Santos, Phys. Rev. Lett. **107**, 270401 (2011).
[29] G. V. Chester, Phys. Rev. A **2**, 256 (1970).
[30] A. L. Fetter and J. D. Walecka, *Quantum Theory of Many-Particle Systems* (Dover Publications, Mineola, New York, 2012).
[31] U. R. Fischer, Phys. Rev. A **73**, 031602(R) (2006).
[32] L. Pitaevskii and S. Stringari, *Bose-Einstein Condensation and Superfluidity* (Oxford University Press, New York, 2016).
[33] See Supplemental Material at http://link.aps.org/supplemental/10.1103/3646-v33q for additional details on the free energy computation methodology, the superfluid fraction finite-size scaling analysis, and the density structure factor Bogoliubov analysis.
[34] T. G. Kiely, E. C. McGarrigle, and G. H. Fredrickson, Phys. Rev. A **113**, 023310 (2026).
[35] G. H. Fredrickson, K. T. Delaney, G. H. Fredrickson, and K. T. Delaney, *Field-Theoretic Simulations in Soft Matter and Quantum Fluids*, International Series of Monographs on Physics (Oxford University Press, Oxford, New York, 2023).
[36] E. C. McGarrigle, K. T. Delaney, L. Balents, and G. H. Fredrickson, Phys. Rev. Lett. **131**, 173403 (2023).
[37] E. C. McGarrigle, R. Nodel, K. T. Delaney, L. Balents, and G. H. Fredrickson, Phys. Rev. A **110**, L041303 (2024).
[38] R. Barnett, S. Powell, T. Graß, M. Lewenstein, and S. Das Sarma, Phys. Rev. A **85**, 023615 (2012).
[39] R. Liao, Phys. Rev. Lett. **120**, 140403 (2018).
[40] G. H. Fredrickson and K. T. Delaney, Proc. Natl. Acad. Sci. U.S.A. **119**, e2201804119 (2022).

[41] C.-M. Jian and H. Zhai, Phys. Rev. B **84**, 060508(R) (2011).
[42] D. R. Nelson and B. I. Halperin, Phys. Rev. B **19**, 2457 (1979).
[43] M. Clausse, J. Peyrelasse, J. Heil, C. Boned, and B. Lagourette, Nature (London) **293**, 636 (1981).
[44] S.-W. Su, I.-K. Liu, Y.-C. Tsai, W. M. Liu, and S.-C. Gou, Phys. Rev. A **86**, 023601 (2012).
[45] A. P. Lindsay, R. M. I. Lewis, B. Lee, A. J. Peterson, T. P. Lodge, and F. S. Bates, ACS Macro Lett. **9**, 197 (2020).
[46] 10.5061/dryad.s1rn8pkpv
[47] G. Parisi, Phys. Lett. **131B**, 393 (1983).
[48] J. R. Klauder, J. Phys. A **16**, L317 (1983).
[49] K. Jiang, J. Tong, P. Zhang, and A.-C. Shi, Phys. Rev. E **92**, 042159 (2015).
[50] K. Jiang and P. Zhang, J. Comput. Phys. **256**, 428 (2014).
[51] N. Q. Burdick, Y. Tang, and B. L. Lev, Phys. Rev. X **6**, 031022 (2016).
[52] P. Barral, M. Cantara, L. Du, W. Lunden, J. de Hond, A. O. Jamison, and W. Ketterle, Nat. Commun. **15**, 3566 (2024).
[53] M. Lu, N. Q. Burdick, S. H. Youn, and B. L. Lev, Phys. Rev. Lett. **107**, 190401 (2011).
[54] A. Recati and S. Stringari, Nat. Rev. Phys. **5**, 735 (2023).
[55] Y. Tang, A. Sykes, N. Q. Burdick, J. L. Bohn, and B. L. Lev, Phys. Rev. A **92**, 022703 (2015).
[56] I. Ferrier-Barbut, M. Wenzel, F. Böttcher, T. Langen, M. Isoard, S. Stringari, and T. Pfau, Phys. Rev. Lett. **120**, 160402 (2018).
[57] T. Lahaye, J. Metz, B. Fröhlich, T. Koch, M. Meister, A. Griesmaier, T. Pfau, H. Saito, Y. Kawaguchi, and M. Ueda, Phys. Rev. Lett. **101**, 080401 (2008).

End Matter

Field-theoretic simulation details—Our simulation technique consists of sampling the coherent state field theory numerically by evolving the complex Langevin process forward in fictitious Langevin time t [34,36],

$$\frac{\partial}{\partial t}\tilde{\phi}_{\alpha,j}(\mathbf{r},t) = -\frac{\delta S[\tilde{\phi},\tilde{\phi}^*]}{\delta\tilde{\phi}^*_{\alpha,j}(\mathbf{r},t)} + \eta_{\alpha,j}(\mathbf{r},t),$$
$$\frac{\partial}{\partial t}\tilde{\phi}^*_{\alpha,j}(\mathbf{r},t) = -\frac{\delta S[\tilde{\phi},\tilde{\phi}^*]}{\delta\tilde{\phi}_{\alpha,j}(\mathbf{r},t)} + \eta^*_{\alpha,j}(\mathbf{r},t), \tag{A1}$$

where Gaussian white noises are constructed from real noise fields $\eta^{(a)}_{\alpha,j}(\mathbf{r})$ and $\eta^{(b)}_{\alpha,j}(\mathbf{r})$ such that $\eta_{\alpha,j} = \eta^{(a)}_{\alpha,j} + i\eta^{(b)}_{\alpha,j}$ and $\eta^*_{\alpha,j} = \eta^{(a)}_{\alpha,j} - i\eta^{(b)}_{\alpha,j}$, where $\langle\eta^{(a)}_{\alpha,j}(\mathbf{r},t)\rangle = 0$ and $\langle\eta^{(a)}_{\alpha,j}(\mathbf{r},t)\eta^{(a')}_{\gamma,j'}(\mathbf{r}',t')\rangle = \delta_{a,a'}\delta_{\alpha,\gamma}\delta_{j,j'}\delta(\mathbf{r}-\mathbf{r}')\delta(t-t')$. The functional derivatives in Eq. (A1) refer to first variations of the action functional detailed in Eq. (3). To integrate the equations (A1) forward in time, an exponential-time-differencing algorithm with Langevin time discretization Δt propagates the SOC forces exactly to all orders in Δt. Additionally, the interaction terms are treated by a second-order-accurate Runge Kutta scheme [35] that requires $\Delta t < 0.01$ for accurate results in this model. The pseudospectral method uses plane-wave collocation and periodic boundary conditions in both spatial and imaginary time domains, where the fields live on a computational lattice (N_x, N_y, N_τ) and spatial domain $r_\nu \in [0, L_\nu]$ for directions $\nu = x,\ y$. Such an approach is computationally exact when (N_x, N_y, L_x, L_y, N_τ) are chosen to be large enough and Δt small enough to drive down discretization errors and converge thermodynamic properties. Stationary solutions of Eq. (A1) implicitly sample the stationary distribution governing the finite-temperature theory, which permit the calculation of expectation values via long-time sample averaging [47,48].

This approach accesses a periodic approximant of the quasicrystal phase, requiring large simulation cells to prevent simulation artifacts from the periodic boundary conditions [49,50]. To find the system size required to access the QC phase for a particular SOC strength $\bar{\kappa}$, we parametrize the simulation cell length $\bar{L}_\nu(n) = n\bar{\lambda}_{\mathrm{SOC}}$ by the number n of SOC length scales $\bar{\lambda}_{\mathrm{SOC}} \equiv \lambda_{\mathrm{SOC}}/\ell = 2\pi/\bar{\kappa}$. For a square cell, increasing n will increase the system size (area) quadratically via $A = \ell^2(2\pi n/\bar{\kappa})^2$. Correspondingly, increasing n at fixed $\bar{\kappa}$ leads to a finer momentum space resolution $\Delta\bar{k}_\nu = 2\pi/\bar{L}_\nu = \bar{\kappa}/n$. We determined that the octagonal QC phase is accessible by choosing a square grid $\bar{L} = \bar{L}_x = \bar{L}_y$ and setting $n > 110$ for $\bar{\kappa} = 16$ or equivalently $\Delta\bar{k}_\nu < 0.13$. Supplemental Material [33] demonstrates the system-size independence of the free energy estimates for these large simulations cells ($n \geq 120$).

Accurate estimates of thermodynamic properties requires a sufficient wave vector cutoff $k_{\max} \equiv N_x\pi/\bar{L} > 3\bar{\kappa}$, or equivalently a fine spatial resolution $N_x = N_y \geq 6n$. This resolution requirement corresponds to a dimensionless grid spacing of $\Delta\bar{x} = \Delta\bar{y} = \bar{L}/N_x < \pi k^{-1}_{\max}$. Therefore, as we increase system size by varying n, we compensate by increasing the number of spatial grid points N_x and N_y to satisfy the resolution requirement. In the imaginary time coordinate, we find convergence when choosing N_τ such that $\Delta_\tau < 0.005$ from our previous benchmarking in [34].

Omitting noise from scheme (A1) will drive field configurations to a mean-field saddle point solution. Before conducting a Langevin simulation, defect-free structures are found by a mean-field analysis: using a variational ansatz for a BEC with M-fold symmetry (detailed in [33]), scheme (A1) is evolved without noise until the action variations vanish within a tolerance. After obtaining a defect-free configuration, a simulation box scaling optimization is performed until thermodynamically consistent free energy estimates are achieved, with an example shown in [33]. Then, the corresponding saddle point configuration at the optimal simulation cell condition initializes the stochastic Langevin trajectories to study the finite-temperature structure and thermodynamics of dipolar Rashba Bose gases.

Realization in dysprosium gases—Here, we discuss a possible realization of the octagonal quasicrystal in ^{164}Dy quantum gas experiments [51–54], which naturally achieve a dipolar dominant regime: $R \in [1.38, 1.88)$ [32]. The precise dipolar parameter value depends on the s-wave scattering length a_s, ranging from $92a_0$ ($R \sim 1.38$) [55] to $69a_0$ ($R \sim 1.48$) [56] with Bohr radius a_0, where $R > 1.48$ requires decreasing a_s via Feshbach resonance techniques [57]. Strong SOC can be achieved by using a 626 nm laser to drive Raman transitions between large hyperfine spin states $m_F = 7, 8$ with $\kappa = \sqrt{2}\pi/\lambda_{\text{laser}}$.

One possible experiment would access different regions of the phase diagram in Fig. 3 by modulating the axial length scale $\bar{d}_z$ by changing the axial trap frequency ω_z. Fixing $R = 1.38$, changing d_z will shift R_M in Eq. (5), such that each phase may be accessed. For example, an axial trap frequency of $\omega_z \sim 150$ Hz $\times 2\pi$ corresponds to $\bar{\kappa}\bar{d}_z \sim 4$ and would support observing the octagonal QC at $R \sim 1.38$. Such an experiment would observe the hexagonal and square BEC phases by increasing the axial trap frequency by a factor of 2 and 4, respectively. For a system with 10^5 atoms ($\mu_{\text{eff}}/h = 0.5$ kHz), we estimate from Fig. 3 that the hexagonal-octagonal transition at $R \sim 1.4$ would occur at $T_{c1} \sim 75$ nK, while the hexagonal-to-isotropic transition would occur near $T_{c2} \sim 210$ nK.